Polymer 54 (2013) 4194–4203

Contents lists available at SciVerse ScienceDirect

Polymer

journal homepage: www.elsevier.com/locate/polymer

Enhanced properties of polyurea elastomeric nanocomposites with anisotropic functionalised nanofillers

Adriana M. Mihut [a,b,1], Antoni Sánchez-Ferrer [c,1], Jérôme J. Crassous [a,b], Liliane Ackermann Hirschi [a], Raffaele Mezzenga [c], Hervé Dietsch [a,d,*]

[a] Adolphe Merkle Institute and Fribourg Center for Nanomaterials, University of Fribourg, Route de l'Ancienne Papeterie, P.O. BOX 209, CH-1723 Marly 1, Fribourg, Switzerland
[b] Physical Chemistry, Department of Chemistry, Lund University, 22100 Lund, Sweden
[c] ETH Zurich, Department Health Sciences and Technology, Institute of Food, Nutrition & Health, Food & Soft Materials Science Group, Schmelzbergstrasse 9, LFO, E23-E29, CH-8092 Zurich, Switzerland
[d] BASF SE, Formulation Platform, 67056 Ludwigshafen am Rhein, Germany

ARTICLE INFO

Article history:
Received 27 January 2013
Received in revised form
24 May 2013
Accepted 24 May 2013
Available online 4 June 2013

Keywords:
Nanocomposites
Mechanical properties
Elastomers

ABSTRACT

We report on the network characterization of a series of hybrid nanocomposites consisting of integrated anisotropic nanoparticles (NPs) within a polyurea elastomeric matrix with low weight fractions ranging from 0.3 to 1.2 wt%. The grafting method employed to incorporate the silica-coated spindle-type hematite nanoparticles (SCH NPs), promotes the stability of the NPs in dispersion, and further enables their integration within the elastomeric polymer matrix, where the NPs are acting as multifunctional chemical crosslinkers and reinforcing fillers. The mechanical properties of these nanocomposite materials have systematically been investigated for both small and large deformations as a function of the particles concentration in the matrix. The results indicate that significant reinforcement of the hybrid nanocomposite is achieved even at very low NP loading with respect to the pristine elastomeric matrix.

1. Introduction

Polymeric nanocomposite materials consisting of a polymer matrix and a nanosized filler component are intensely investigated, in the search for innovative materials with improved properties and a tuneable response to external stimuli. This class of materials is interesting for a broad range of applications, due to their thermo-mechanical, magnetic, electrical and optical properties on the one hand, and to their chemical stability, easy processing, sustainability (chemical footprint) and low cost on the other hand [1–7]. These unique and specific properties depend on many factors such as the filler characteristic size, shape, anisotropy, concentration, chemical nature and polymer/filler interaction potential [8–13]. It is well known that the incorporation of fillers into the polymer matrix deeply modifies the mechanical properties of the pristine network, mainly because of the creation of interfaces. Reinforcing effects have been already reported in literature [14,15], and the mechanical properties can be strongly controlled by the following parameters: (i) the nature of the interactions between the polymer chains and the particle surface, (ii) the volume fraction of the filler particles, and (iii) the quality and stability of the dispersion and distribution of the filler particles [16]. The reinforcing influence of the filler on the mobility of the polymer chains is one of the most studied topics in the last decade, in the field of elastomers [17–22]. In particular, in the case of rubber, the reinforcement induced by solid particles shows significantly improved mechanical properties (elastic modulus, fracture resistance, abrasion resistance, etc). Moreover, it is reasonable to expect that physical adsorption or chemical attachment of polymer chains to rigid particles can affect the polymer dynamics. In the case of carbon black filled systems, the interactions between the polymer chains and the filler particles surface induces an increased gradient of mobility of the polymer chains from the filler interface to the bulk matrix [17]. The formation of a thin coating of a polymer layer with reduced mobility in the vicinity of the filler surface as immobilised glassy-like polymer has been already reported for silica/rubber composites [16,21–23]. This polymer/particle interface is often designated as the glassy layer, possessing different physical properties than the bulk polymer.

* Corresponding author. BASF SE, Formulation Platform, 67056 Ludwigshafen am Rhein, Germany.
E-mail addresses: herve.dietsch@gmail.com, herve.dietsch@basf.com (H. Dietsch).
[1] These authors contributed equally to this work.

0032-3861/$ – see front matter © 2013 Elsevier Ltd. All rights reserved.
http://dx.doi.org/10.1016/j.polymer.2013.05.056

In the presence of strong polymer/filler interactions, when the polymer chain mobility is strongly hindered around the filler, glassy-like polymer bridges between adjacent filler particles are formed. These bridges are mainly responsible for the transmission of stress by the filled elastomer network [24–26]. Small filler particles and strong polymer/filler interactions increase the volume fraction of immobilised interfacial layers, which in turn increases the overall glass transition temperature of the sample, due to the high surface to volume ratio of the nanofillers [17,27]. Strong reinforcement of nanofilled elastomers and thermoplastic elastomers was obtained when glassy layers between the fillers overlapped [26]; this effect is particularly strong when the corresponding clusters/fillers and glassy layers percolate. The presence of overlapping layers results in a high level of stress with finite lifetimes between the fillers, which depends on the thermal, compounding and preparation history of the sample. Moreover, the formation of strong rubber/filler interactions leads to a reduction of the swelling capacity of the polymer network, as the non-swellable filler particles are macroscopic crosslinkers which create an inhomogeneous strain field in the nanocomposite in the swollen state [20]. In this sense, the interfacial characteristics of the filler particles (e.g., the formation of glassy layers, the effective filler volume fraction, the dispersibility, and the aggregation degree) are considered to be the main factors determining the improvement of the mechanical properties and the restrictions of the swelling capacity of the final composite.

If grafted nanoparticles (NPs) are used for the reinforcement of the polymer matrix, the interactions will depend on the nature of the coupling agent used to cover the NPs surface. Moreover, this reinforcement is strongly affected by the NPs arrangement in the matrix, which is often dispersed as fractal aggregates. Incorporation of large amounts of NPs into polymer matrices is one of the most crucial conditions to obtain strong and uniform responses of the nanocomposite material [9–11,28–32]. Aggregation problems are usually overcome by surface modification of the NPs, improving the interactions with the polymer and therefore enhancing the reinforcement effect. Additionally, another parameter which influences the mechanical properties of nanocomposites is the quality of the dispersion state of the NPs which can be enhanced by changing the chemistry of the NPs surface. Model nanocomposites are widely reported in literature, however, only few examples exist with well-dispersed and well-distributed NPs within the polymeric matrix.

In our previous studies, we reported the development of a new synthetic approach which allows to achieve hybrid nanocomposite elastomers via efficient control of surface-functionalised silica-coated hematite nanoparticles (SCH NPs) [33,34]. In the present work, the mechanical and thermo-mechanical properties of different iron oxide elastomer nanocomposites (IOENs) are systematically studied while varying the amount of crosslinkable NPs in the networks. The dispersed filler SCH NPs are anisotropic with long and short axes around 354 nm and 92 nm, respectively, and possess considerable surface area. The structure and the colloidal dispersion of these magnetic NPs in solution and in the polymer matrix have been investigated by a combination of Small Angle X-ray Scattering (SAXS), Dynamic Light Scattering (DLS) and Transmission Electron Microscopy (TEM).

The synthetic steps procedure, which will affect and determine the affinity of the NPs within the elastomeric matrix is discussed in details by investigating the mechanical properties of the synthesised IOENs. The mechanical response of the corresponding nanocomposite has been investigated as a function of the filler content at low (Dynamical Mechanical Analysis, DMA) and large deformations (uniaxial stress–strain deformation). Finally, the contribution of the physical and chemical crosslinking points on the mechanical properties of the nanocomposite material have also been investigated.

2. Experimental section

2.1. Synthesis of iron oxide elastomeric nanocomposites

Surface-functionalised silica-coated hematite nanoparticles (SCH NPs) were obtained in a first step following a previously reported method [35]. The surface modification was done using 3-aminopropyltriethoxysilane (APTES) as coupling agent (ABCR, Germany), used without previous purification. In a typical example, 300 mg of SCH NPs were suspended in 1 L of absolute ethanol (Merck), and 160 μL of APTES were added to the mechanically stirred suspension under sonication for 2 h at 25 °C. After stirring the suspension overnight, the obtained amino-functionalised SCH NPs were centrifuged at 10,000 rpm for 15 min, redispersed in acetone (Merck); the process was repeated five times. Three iron oxide elastomer nanocomposites (IOENs) were synthesised adapting our previously developed and reported procedure [33,34]. An elastomer which did not contain any NPs (E0) was synthesised as a reference [36]. The elastomeric matrix was obtained combining a diamino-terminated poly(propylene oxide), Jeffamine D-2000, $M_n = 2000$ g mol^{-1} (Huntsman Corporation), with a triisocyanate crosslinker, Basonat HI-100 (BASF SE), $mw = 505$ g mol^{-1} (Fig. SI-1). For the synthesis of the reference and the model IOENs, four times 3.865 g (1.25 mmol) of Jeffamine D-2000 were dissolved in 6.94 mL of acetone and 0.63 g (1.88 mmol) of Basonat HI-100 were added to 9.05 mL of acetone containing respectively 0 mg, 15 mg, 30 mg, and 60 mg of functionalised SCH NPs. After 2 h at room temperature, both the polymer and the crosslinker/SCH NPs solutions were mixed and poured in Petri dishes, allowing them to react for 1 day. Acetone was slowly removed by evaporation at room temperature, and the resulting elastomeric films were peeled off. The three IOENs contained 0.3 wt% (E1), 0.6 wt% (E2) and 1.2 wt% (E3) of SCH NPs. For the mechanical experiments, samples were cut from their corresponding free-standing films.

2.2. Apparatus and techniques

A Leica DM LB optical microscope equipped with a Linkam CSS450 hot stage was used to image the dispersion efficiency of the SCH NPs within the elastomeric matrix.

Small Angle X-ray Scattering (SAXS) experiments were carried out at the cSAXS (X12SA) beam line at the Swiss Light Source (Paul Scherrer Institute, Villigen, Switzerland). The beam line energy was set to 11.2 keV (corresponding to a wavelength of $\lambda = 0.1514$ nm) for all the experiments, which enabled a large q range going from 0.01 to 1 nm^{-1}, where $q = 4\pi\sin\theta/\lambda$ with 2θ the scattering angle. Isotropic scattering data were obtained using standard procedures. In order to subtract the contribution of the polymer matrix, the pure elastomer E0 without magnetic particles was measured, and its radial scattering intensity distribution was subtracted from all the nanocomposite samples. SCH NPs suspended in ethanol were measured in 1.0 mm quartz capillaries at 20 C, where both the scattering of the solvent and the capillary were removed by subtraction from the raw data.

Dynamic Light Scattering (DLS) measurements were carried out on a 3D LS spectrometer (LS Instrument) equipped with a He–Ne laser ($\lambda = 633$ nm). The measurements were performed on 0.01 wt% SCH NPs solution in ethanol. To investigate the step procedure for the surface functionalisation of the SCH NPs and their integration into the polymer matrix, NP samples were prepared following the same procedure as described for the synthesis of the E1 nanocomposite, and containing 15 mg of functional SCH NPs (0.3 wt%

SCH NPs). The solutions in acetone corresponding to each synthetic step, such as functionalised APTES-SCH NPs, functionalised crosslinker-SCH NPs and the polymer-grafted SCH NPs were measured at scattering angles ranging from 45° to 135° with a step of 15°. The resulting apparent hydrodynamic radius was evaluated from the first cumulant analysis.

Stress–strain measurements were performed on a Linkam TST350 thermostated tensile testing system controlled by a T95-LinkSys apparatus. Uniaxial deformation was set at an extension rate of 10 μm min^{-1} which corresponds to a strain rate of 1.14 10^{-5} s^{-1}.

Dynamic Mechanical Analysis (DMA) data were measured for the different IOENs and the reference polymer matrix. The DMA measurements were carried out on a TA Instruments DMA Q800 equipped with a liquid nitrogen cooling apparatus. Scans were performed for intervals starting with an initial temperature of −90 °C heated to 110 °C and cooled again to −90 °C at a constant heating/cooling rate of 5 K min^{-1} under nitrogen atmosphere. Samples were cut into rectangular pieces (8.5–12.5 mm × 8–9 mm and 0.7–0.9 mm thickness). Measurements were performed at a fixed frequency of 1 Hz and a fixed oscillation displacement of 20 μm. For the isothermal frequency-sweep experiments, the mechanical evolution of all samples was recorded as function of frequency ranging from 0.01 to 200 Hz. Samples were investigated after 20 min of thermal equilibration.

Differential Scanning Calorimetry (DSC) experiments were performed on a Mettler Toledo DSC calorimeter equipped with a Huber TC100 cooling system. The nanocomposites were encapsulated in 40 μL aluminium oxide crucibles and measured under nitrogen atmosphere in a temperature range from −80 to 150 °C at a scanning rate of 10 K min^{-1}. This cycle was performed twice to check the reversibility of the transitions.

Transmission Electron Microscopy (TEM) images were obtained using a Philips TEM (CM100) microscope operated at 80 kV. Samples were prepared by placing 4 μL droplet of the 0.1 wt% and 0.3 wt % SCH NPs ethanol and acetone dispersions, respectively, onto a carbon-coated copper grid.

Swelling experiments were performed at room temperature and using acetone as a solvent, and the swelling parameter was evaluated as a ratio of the initial to final dimensions of the samples.

3. Results and discussion

3.1. Synthesis and characterization of iron oxide elastomeric nanocomposites

The reference elastomer (E0) and the three IOENs containing 0.3 wt% (E1), 0.6 wt% (E2) and 1.2 wt% (E3) of SCH NPs were synthesised following the procedure already described in the Experimental Part. The three IOENs were obtained by mixing the corresponding isocyanate-functionalised particles dispersion together with the diamino-terminated polymer solution in acetone, which subsequently form a swollen gel network after the complete crosslinking process between the amino groups and the excess of isocyanate molecules and the functionalised NPs.

In order to check the quality of the films, optical microscopy experiments were performed. These SCH NPs are red, therefore the three IOEN films showed a colour gradient from pale to dark red as function of the increasing amount of NPs. Fig. 1 shows the optical microscopy images of the transparent reference elastomeric matrix E0 and the three different red coloured IOEN samples E1, E2 and E3. Their macroscopically homogeneous quality was an indication of the good dispersion of the NPs within the elastomeric matrix.

The microscopic assessment of the IOEN films can be confirmed by Small Angle X-ray Scattering (SAXS) experiments. Thus, SAXS

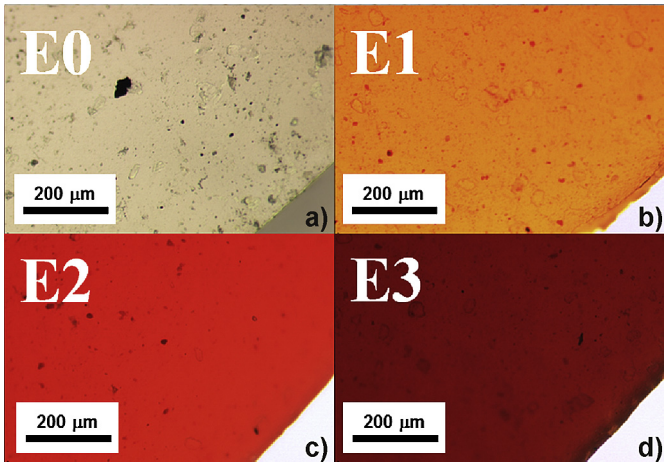

Fig. 1. Optical microscopy images of the (a) reference elastomer E0, and the three IOENs with increased concentration of SCH NPs: (b) 0.3 wt% E1, (c) 0.6 wt% E2 and (d) 1.2 wt% E3.
Note: the light intensity was the same for all IOENs, but lower for the reference sample for better contrast.

experiments were performed on 0.1 wt% SCH NPs dispersed in ethanol and on the IOEN films in order to check the final quality and estimate the amount of NPs in the elastomeric films. Fig. 2a shows the 1D scattering curves for the SCH NPs dispersion and for the three IOEN samples, which have the same scattering profile and increased intensity when increasing the amount of NPs into the elastomeric matrix.

Prior to embedding the SCH NPs into the polymer matrix, size and shape were investigated by determining the corresponding form factor, $P(q)$. Since these core–shell SCH NPs are ellipsoidal, their scattering profile should be well-described by the form factor of a prolate core–shell ellipsoidal model as follows [37,38]:

$$I(q) = N_p \int_0^1 \left| V_{core}(\rho_{shell} - \rho_{core}) \frac{3j_1(u_{core})}{u_{core}} + V_{shell}(\rho_{solv} - \rho_{shell}) \frac{3j_1(u_{shell})}{u_{shell}} \right|^2 d\alpha + bkg \quad (1)$$

$$u_x = q\left[r_{x,maj}^2\alpha^2 + r_{x,min}^2\left(1-\alpha^2\right)\right]^{1/2} \quad (2)$$

$$V_x = \frac{4\pi}{3} r_{x,maj} r_{x,min}^2 \quad (3)$$

$$j_1(x) = \frac{(\sin x - x\cos x)}{x^2} \quad (4)$$

where N_p is the number of particles per unit volume, V_x is the volume, ρ_x is the scattering length density, $r_{x,maj}$ is the ellipsoidal major radius, $r_{x,min}$ is the ellipsoidal minor radius, $j_1(x)$ is the first order spherical Bessel function, and bkg is the instrumental background (α is an integration variable). The best fit of the SAXS data for the SCH NPs was obtained when taking into account a polydispersity value of 0.13 for a particle size distribution with a major core radius of $r_{core,maj}$ = 155 nm, a minor core radius of $r_{core,min}$ = 24.6 nm, a major shell radius of $r_{shell,maj}$ = 176.8 nm, and a minor shell radius of $r_{shell,min}$ = 44.1 nm, and by fixing the values for the scattering length densities ρ_{hem} = 4.2965 × 10^{-3} nm^{-2} (d_{hem} = 5.260 g cm^{-3}) and $\rho_{ethanol}$ = 7.6425 × 10^{-4} nm^{-2}

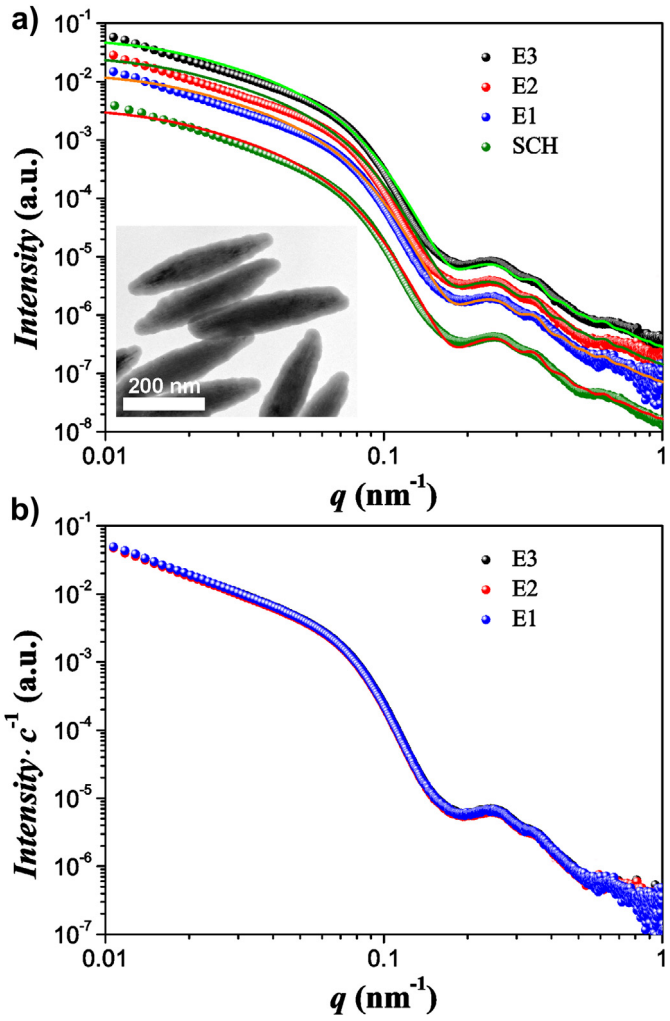

Fig. 2. (a) Intensity scattering profiles of the SCH NPs dispersion, and the three IOENs (E1, E2 and E3) normalised by their background (ethanol and the polyurea matrix, respectively). The inset shows a TEM image of the SCH NPs. The continuous lines represent the fit by the form factor function $P(q)$ given by Equation (1). (b) 1D radial scattering distribution of the three IOEN samples corrected and normalised by their corresponding SCH NPs filler content.

($d_{ethanol} = 0.789$ g cm^{-3}). For the case of the silica shell, a scattering length density of $\rho_{silica} = 1.7653 \times 10^{-3}$ nm^{-2} ($d_{silica} = 2.06$ g cm^{-3}, expected for Stöber-like silica) was considered [39]. The size distribution of the minor and major axes was obtained from a Gauss-fit of the statistical histogram from TEM images performed for 150 SCH NPs, showing values of $r_{core,maj} = 155$ nm, $r_{core,min} = 27.6$ nm, $r_{shell,maj} = 176.8$ nm, and $r_{shell,min} = 46.1$ nm (Fig. 2a inset).

Since the SCH NPs dispersion and the three IOENs presented similar SAXS profiles, all scattering curves from the films were fitted with the same core–shell prolate ellipsoidal model but taking into account the scattering length density for the polyurea matrix $\rho_{matrix} = 9.4585 \times 10^{-4}$ nm^{-2} ($d_{matrix} = 1.002$ g cm^{-3}) as a fix parameter. The particles' dimensions obtained from the best fit showed identical values to those from the SCH NPs dispersion in ethanol, demonstrating that the form factor of the NPs remains the same after transferring them into the elastomer matrix.

The SAXS intensity profiles are mainly dominated by the contrast between the inorganic particles and the polymer matrix, and are directly related to the NPs concentration in the sample. Fig. 2b shows the normalised scattering curves by the filler content, where all the three scattering curves perfectly superimpose to the form factor of the NPs. Therefore, based on the SAXS analysis, it can be concluded that no significant changes in the particle dispersion occurred in the IOEN films containing different concentrations of NPs, and their aggregation is negligible at the filler content concentration investigated. A slight increase in the scattering profile at low q values indicates the presence of a limited amount of aggregates. This increase was not accentuated for the IOEN samples versus the measured reference form factor obtained from the SCH NPs dispersed in ethanol, showing that the process for the surface modification using APTES plays an important role in the dispersion and distribution of the NPs acting as multi-crosslinker NPs [33]. However, from our experience, aggregation phenomena could be observed at higher filler concentration content, >1.2 wt% (data not presented here). These phenomena related to the increase of the fillers content can be attributed to a possible depletion or to an enhancement of the aggregation rate between the surfaces functionalised NPs. Aggregation phenomena on nanocomposites made of spherical maghemite NPs dispersed in a polystyrene matrix have been reported in a similar work by increasing the filler content [8].

3.2. Compatibility of inorganic nanoparticles within the polymer matrix

In order to ensure a good dispersibility of the engineered inorganic NPs in the composite materials, the particles need to be functionalised. Fig. 3a–d shows the synthetic steps procedure for the surface chemistry used to obtain IOENs, which appears to be crucial for the stability and dispersibility of SCH NPs into the polymer matrix. DLS experiments allowed to follow the different steps of functionalisation, and the translational diffusion coefficient D_T was calculated for each NP. The decay rate Γ was determined from the first cumulant analysis of the field autocorrelation function. D_T was then calculated from the linear extrapolation of Γ versus q^2 (Fig. 3e). The translational diffusion coefficient D_T for prolate particles can be described by the Perrin's formula [40,41]:

$$D_T = \frac{k_B T}{f} \tag{5}$$

$$f = 3\pi\eta L\sqrt{p^2-1}/\left(p\ln\left(p+\sqrt{p^2-1}\right)\right) \tag{6}$$

where f is the translational friction coefficient for a single prolate ellipsoidal particle with random orientation, η is the solvent viscosity, and $p = L/d$ is the aspect ratio ($p > 1$) for a prolate ellipsoid with a long axis L and a short axis d.

Following the approach described in a recent study on similar particles [41], D_T was estimated from the statistics of TEM pictures over 100 analysed particles. As the scattered intensity is proportional to the square of the volume of a single particle, the corresponding weighting follows:

$$\langle D\rangle = \frac{\sum D_i v_i^2}{\sum v_i^2} \tag{7}$$

where D_i and V_i are the translational diffusion coefficients and volumes of each single particle in the data set, respectively. The computed value determined for the bare SCH NPs dispersed in ethanol ($\eta = 1.2 \times 10^{-3}$ Pa s) was $D_T = 2.037 \times 10^{-12}$ m^2 s^{-1}. The good agreement with the experimental value of $D_T = 1.91 \times 10^{-12}$ m^2 s^{-1} (Fig. 3e, black circles) confirmed the good dispersion of the particles in this medium, and the validity of the model where the SCH NPs have a hydrodynamic shape of an ellipsoid (Fig. 3a) with the dimensions close to those estimated

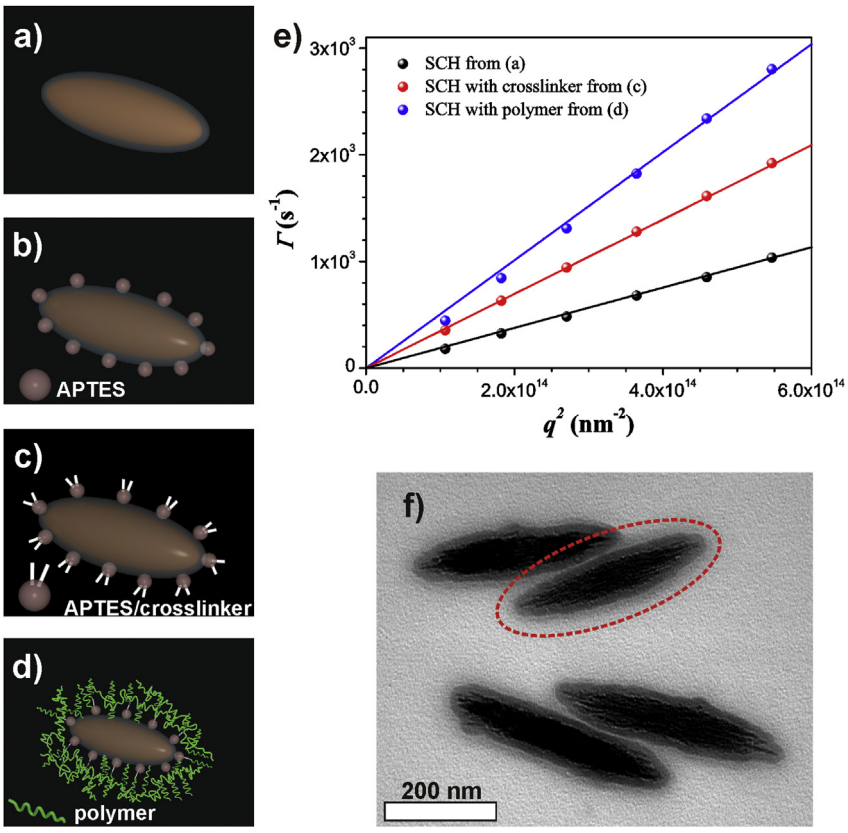

Fig. 3. Schematic illustration of the synthetic procedure for covalent surface chemistry on silica-coated hematite nanoparticles (SCH NPs): (a) bare SCH NPs, (b) APTES-functionalised SCH NPs, (c) isocyanate-functionalised crosslinkable SCH NPs, (d) amino-terminated polymer-decorated SCH NPs. (e) Decay rates Γ as a function of the squared scattering vector q^2, for the SCH NPs in ethanol (black circles), isocyanate-functionalised crosslinkable SCH NPs in acetone (red circles), and amino-terminated polymer-decorated SCH NPs in acetone (blue circles). (f) TEM micrograph of the amino-terminated polymer-decorated SCH NPs. The ellipse around the entire particle provides the estimated hydrodynamic dimension of the particle from the DLS analysis (For interpretation of the references to colour in this figure legend, the reader is referred to the web version of this article).

from the TEM analysis (Fig. 3f). While the bare SCH NPs are stable in ethanol, they are becoming unstable in acetone ($\eta = 3.2 \times 10^{-4}$ Pa s) after the surface modification with APTES (Fig. 3b). As a consequence, the measured $D_T = 8.60 \times 10^{-13}$ m^2 s^{-1} is much lower than the calculated prediction of $D_T = 7.64 \times 10^{-12}$ m^2 s^{-1}, revealing the presence of large aggregates.

Considering the existence of a homogeneous coating and the prolate ellipsoidal shape of the SCH NPs (Equations (5)–(7)), the effective hydrodynamic thickness of the polymer layer could be estimated to be 33.8 nm, which was confirmed as well by TEM analysis of the NPs in the dried state (Fig. 3f) with an immobilised thin polymer layer of thickness 23.7 ± 6.64 nm. The IOENs containing up to 1.2 wt% NPs were found to have well-dispersed and well-distributed SCH NPs within the elastomeric matrix. Therefore, this procedure for the integration of well-dispersed NPs into a polymer matrix offers new possibilities for the development of hybrid systems with advanced control over the distribution and dispersion of NPs and avoiding aggregation phenomena. In fact, this is a powerful approach to functionalise silica NPs or silica surfaces with amino groups, offering the possibility to graft polymers, dyes or proteins to the surface of magnetic particles, which could find many biological applications [42].

As previously mentioned, the SCH NPs are surface modified in order to act as multi-crosslinkers, increasing the crosslinking

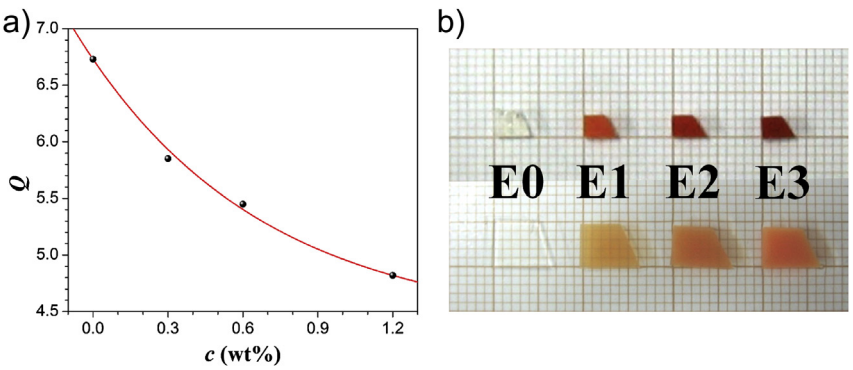

Fig. 4. (a) Volumetric swelling parameter Q for the reference elastomer E0 and the three IOENs E1, E2 and E3 as a function of the NPs concentration. (b) Digital images of the four samples before and after swelling in acetone at 25 °C.

density in their surroundings and, therefore, modifying the swelling and mechanical properties of the final hybrid nanocomposites. The swelling volumetric parameter Q of all elastomeric samples was evaluated, and a decrease in the swelling parameter was observed when increasing the amount of incorporated SCH NPs for the IOENs, as depicted in Fig. 4a. This effect can be explained by the increased crosslinking densities, leading to a reduction in the network mobility as more SCH NPs are incorporated into the polymer matrix. Therefore, multifunctional crosslinkers provide a locally high crosslinking density to the hybrid nanocomposites, whereas the filler increases the rigidity and stiffness of the final material.

3.3. Mechanical behaviour of iron oxide elastomeric nanocomposites

Mechanical analysis of the samples was performed by DMA from −90 °C to 110 °C and back, at a fixed oscillating frequency of 1 Hz. Fig. 5 shows the temperature evolution of the storage modulus E', loss modulus E'' and tan δ for the four elastomeric samples, exhibiting the typical behaviour for a crosslinked elastomeric network with a high E' modulus plateau at low temperatures – related to the glassy state –, followed by two low E' modulus plateaus at intermediate and high temperatures related to two different rubbery states.

The glass transition temperature for all samples was evaluated, showing T_g values ranging from −40 to −46 °C upon heating, and from −69 to −72 °C during cooling as shown from the maxima in tan δ in Fig. 5c. These results were in agreement with those obtained from DSC experiments (Fig. SI-2), where the T_g for the pristine network was around −60 °C [36]. Thus, the presence of SCH NPs has little effect on the glass transition temperature of the samples. Further DMA frequency-sweep measurements showed a maximum in tan δ at −60 °C, confirming the T_g values obtained from DSC experiments.

When temperature increases above the T_g, a steep decrease in the storage modulus E' is observed for all samples, whereas in the high temperature region, the storage modulus E' drops sharply again, reaching an extended plateau. Polyurea elastomers are the combination of chemical and physical crosslinks. The latter ones come from the formation of hydrogen bonds between the urea motives formed during the reaction between isocyanates and amino groups [36]. Thus, at temperatures above T_g and below ca. 70 °C – first plateau –, both the chemical and physical crosslinks are present in the material. At temperatures higher than 70 °C – second plateau –, when no more hydrogen bonds are present, the material becomes softer. Upon cooling the sample, the reformation of these hydrogen bonds only took place at low temperatures (below 0 °C) before the glass transition temperature. This experimental result could be explained due to the difficulty for the urea motives of finding each other and establishing new hydrogen bonds. The physical network is formed again below the glass transition temperature upon cooling the sample.

In Table 1, the storage modulus E' for the four elastomeric samples at different temperatures is shown. In general, the presence of SCH NPs has an effect on the mechanical values in the glassy state (−70 °C), at room temperature (+20 °C) and at temperatures where the hydrogen bonds are not present any longer (+80 °C). When the polymer chains are in a frozen state, the storage modulus is around three orders of magnitude higher than at room temperature, while at high temperatures the mechanical response is about one order of magnitude lower than at ambient conditions. Thus, the presence of supramolecular interactions – hydrogen bonds – enhances ten times the mechanics of the chemical network. At +20 °C, the network is both physically and chemically bonded, and the storage modulus is higher than at +80 °C when the physical

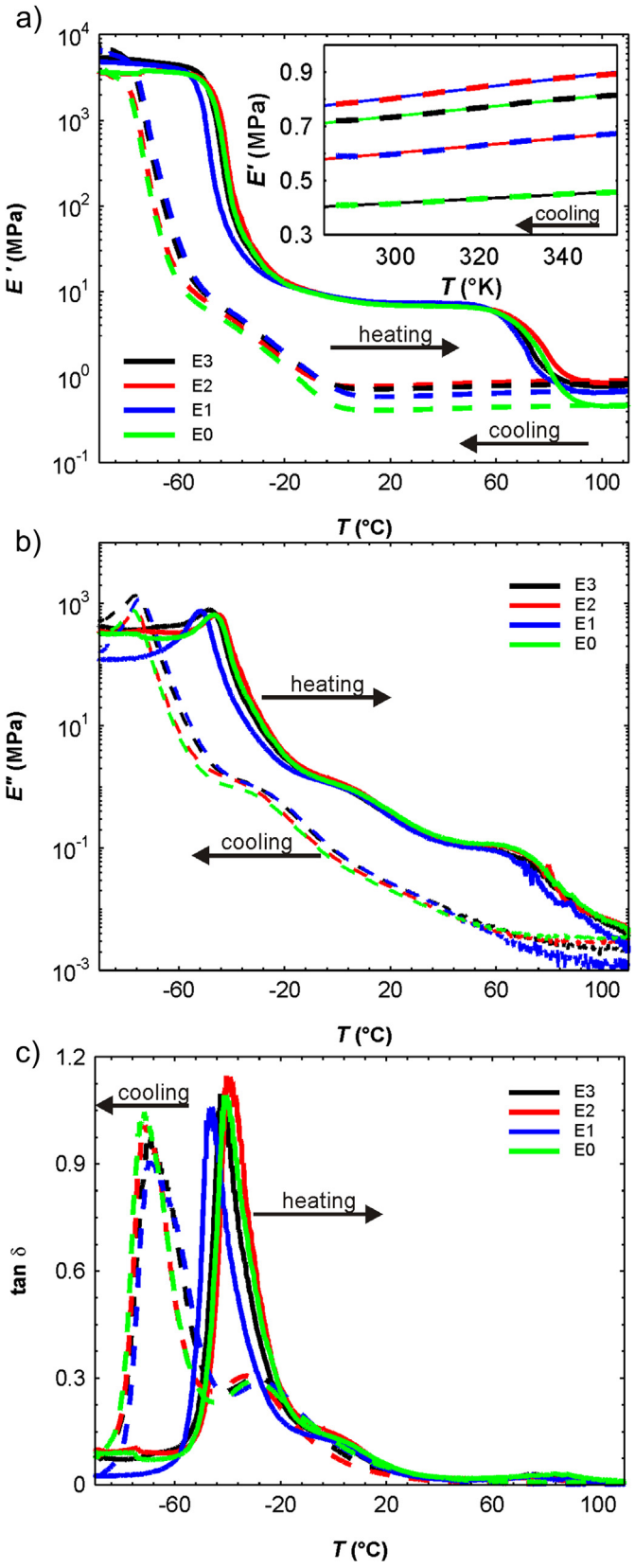

Fig. 5. DMA temperature-sweep measurements at a frequency of 1 Hz showing the (a) storage modulus E', (b) loss modulus E'', and (c) tan δ for the reference elastomer E0 and the three IOENs E1, E2 and E3 as a function of temperature during heating and cooling. The inset in (a) shows the linear increase of E' with temperature upon cooling in the absence of the H-bonding within the rubbery regime.

Table 1
Storage modulus E' from the DMA temperature-sweep and DMA frequency-sweep experiments at −70 °C, +20 °C and +80 °C, and elastic modulus E from the stress–strain experiments at +20 °C for the reference elastomer E0 and the three IOENs E1, E2 and E3.

Sample	E' (MPa)[a]			E' (MPa)[b]			E (MPa)[c]
	−70 °C	+20 °C	+80 °C	−70 °C	+20 °C	+80 °C	+20 °C
E0	3758 (109)	6.95 (0.41)	1.26 (0.46)	2713	4.96	0.35	4.77
E1	4411 (555)	7.40 (0.59)	0.95 (0.67)	3274	6.74	0.52	4.97
E2	3780 (137)	6.98 (0.79)	1.77 (0.89)	3289	6.82	0.73	5.07
E3	4796 (371)	7.34 (0.73)	1.16 (0.82)	3005	6.96	0.64	5.44

[a] Storage modulus from the DMA temperature-sweep experiments; in parenthesis values upon cooling.
[b] Storage modulus from the DMA frequency-sweep experiments at $f = 1$ Hz.
[c] Elastic modulus from the stress–strain experiments.

network – hydrogen bonds – vanishes. When cooling the samples back to +20 °C, the storage modulus remains low, since the hydrogen bonds are still not reformed, as shown from the DMA data (Fig. 5) and DSC experiments (Fig. SI-2). In addition the different elastomeric materials behave as ideal entropic rubbers upon cooling in the rubbery region as E' increases linearly with temperature (see inset in Fig. 5a).

Taking into account the time–temperature superposition principle, it was possible to characterize the dynamic behaviour of the four samples in a large frequency domain. The isothermal storage and loss moduli were obtained as a function of frequency from the DMA frequency-sweep experiments at temperatures where samples are glasses or elastomers. Fig. 6a–c shows the mechanical behaviour of all four samples at −70, +20 and +80 °C, respectively. At −70 °C, all samples are in the glassy state where the storage modulus E' is constant and higher than the loss modulus E''. In the two rubbery plateaux, which are related to the physical and chemical networks (at +20 °C) and to the pure chemical network (+80 °C), the storage modulus E' is also constant and two orders of magnitude higher than the loss modulus E''. Thus, at these two temperatures in the rubbery regimes, all samples behave mainly elastic at the frequency of $f = 1$ Hz. Measurements at intermediate temperatures between the three physical states were also performed (Fig. SI-3) for the construction of the corresponding DMA frequency-sweep master curves.

The extended frequency range obtained by the superposition principle ranged from 10^{-3} to 10^{15} Hz, and the corresponding master curves were obtained using the time–temperature superposition principle (Fig. 6d) [43–45]. Shifting was done on the frequency/tan δ curves, using as reference temperature $T_{ref} = 20$ °C

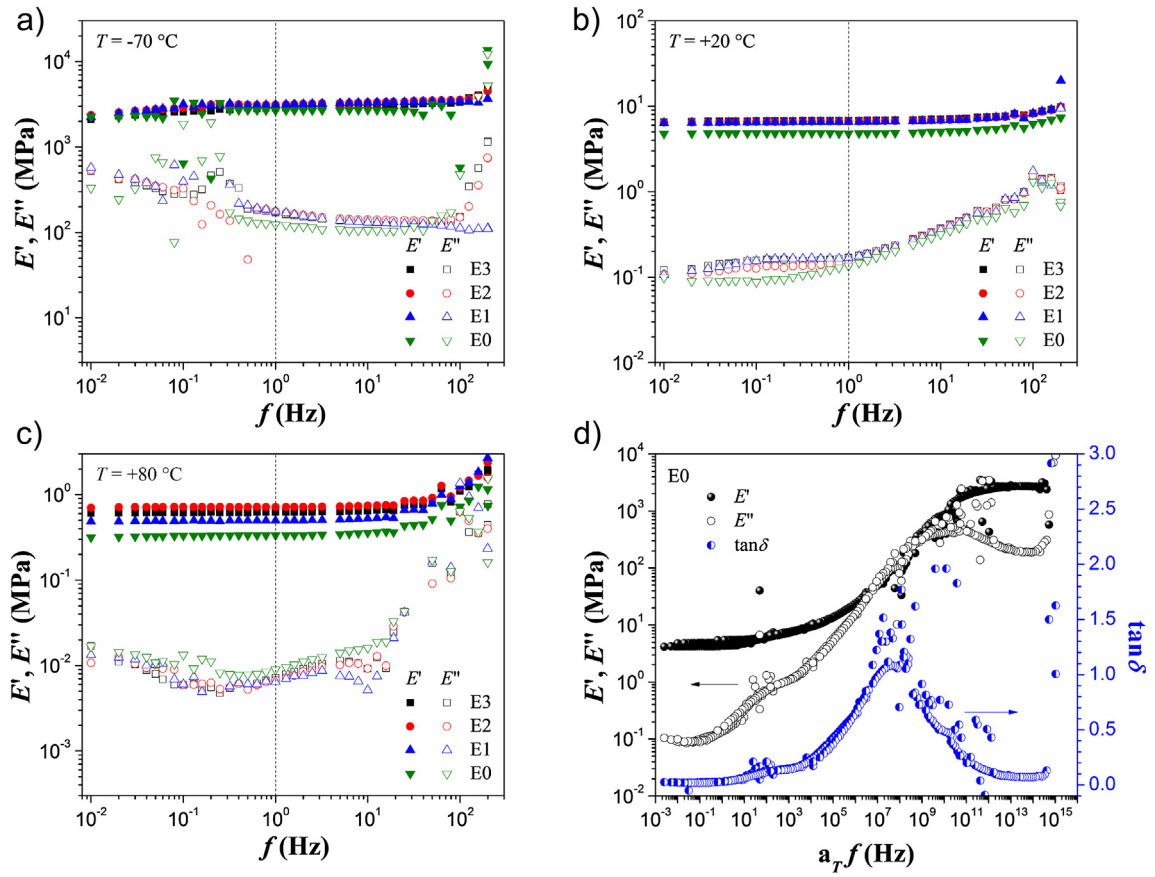

Fig. 6. DMA frequency-sweep measurements for the reference elastomer E0 and the three IOENs E1, E2 and E3 at (a) −70 °C (glassy state), (b) +20 °C (transient rubbery state), and (c) +80 °C (rubbery state). (d) DMA frequency-sweep master curve showing the storage modulus E', the loss modulus E'' and tan δ for the references elastomer E0.

(Fig. SI-4). Thus, the storage and loss moduli were shifted by the same shift factor a_T, which relates the relaxation time at an arbitrary temperature to the relaxation time at the chosen reference temperature based on the Williams–Landel–Ferry (WLF) equation.

$$\log a_T = \log \frac{\tau_T}{\tau_{T_{ref}}} = \frac{-C_1\left(T - T_{ref}\right)}{C_2 + \left(T - T_{ref}\right)} \quad (8)$$

where C_1 and C_2 are the material constants, assumed to be independent from the polymer if similar thermodynamic conditions exist inside the materials. The evolution of a_T as a function of $(T - T_{ref})$, and of C_1 and C_2 determined in the range from $T_g \leq T \leq T_g + 100$ °C with Equation (8) is illustrated in Fig. SI-6 and Table SI-1 for the different materials. The two constants C_1 and C_2, were found to continuously increase with the filler concentration from 4.74 to 6.66, and from 125 to 141 K, respectively.

From the DMA frequency-sweep curves (Fig. 6d and SI-3), it becomes clear that for temperatures around the glass transition temperature ($T_g = -60$ °C), the changes in the storage and loss moduli caused by a change of frequency are higher than at other temperatures, which is characteristic for T_g. Both the storage and loss moduli increase with the decrease of temperature. As the imposed frequency is raised, the storage modulus increases, and all samples appear to be undergoing this transition as an increasing frequency dependence of the master curves at high frequencies was observable in the frequency range of 10^4–10^{15} Hz (Fig. 6d and Fig. SI-5). When going beyond T_g, and increasing the temperature further, the storage modulus decreases when approaching the rubbery states. Therefore, in the case of the filler reinforced elastomers, the low temperature (high frequency regime) mechanical behaviour results from the glassy polymer matrix, whereas at high temperature (low frequency regime) the mechanical response is dominated by the filler, which is significantly stiffer than the polymer matrix. DMA yielded repeatable small variations of both storage and loss moduli for all the samples between the values measured from the DMA temperature-sweep experiments and those determined from the DMA frequency-sweep experiments. Although these values are very similar, it was noticed that the accuracy of these measurements strongly depends on the material's relaxation time and thermal history of the sample.

The storage modulus in the rubbery plateau is an indication of the elastically effective crosslinking density within the polymer network. It has been already reported in literature that the rubbery plateau decreases significantly with the addition of NPs, and the composite networks show higher degree of swelling due to a lower crosslinking density caused by the presence of the NPs [31,32]. Thus, the NPs acted as impurities and were not well integrated in the system. In sharp contrast, in our case the presence on SCH NPs decreases the swelling behaviour (Fig. 4) and enhances the mechanical properties of our IONEs (Table 1) due to the covalent nature of the integration of the NPs into the polymer matrix.

Uniaxial stress–strain deformations were performed in order to evaluate the mechanical properties of all elastomer networks at large deformation values, as well as to compare the results to those based on swelling and DMA experiments. Fig. 7a shows the uniaxial

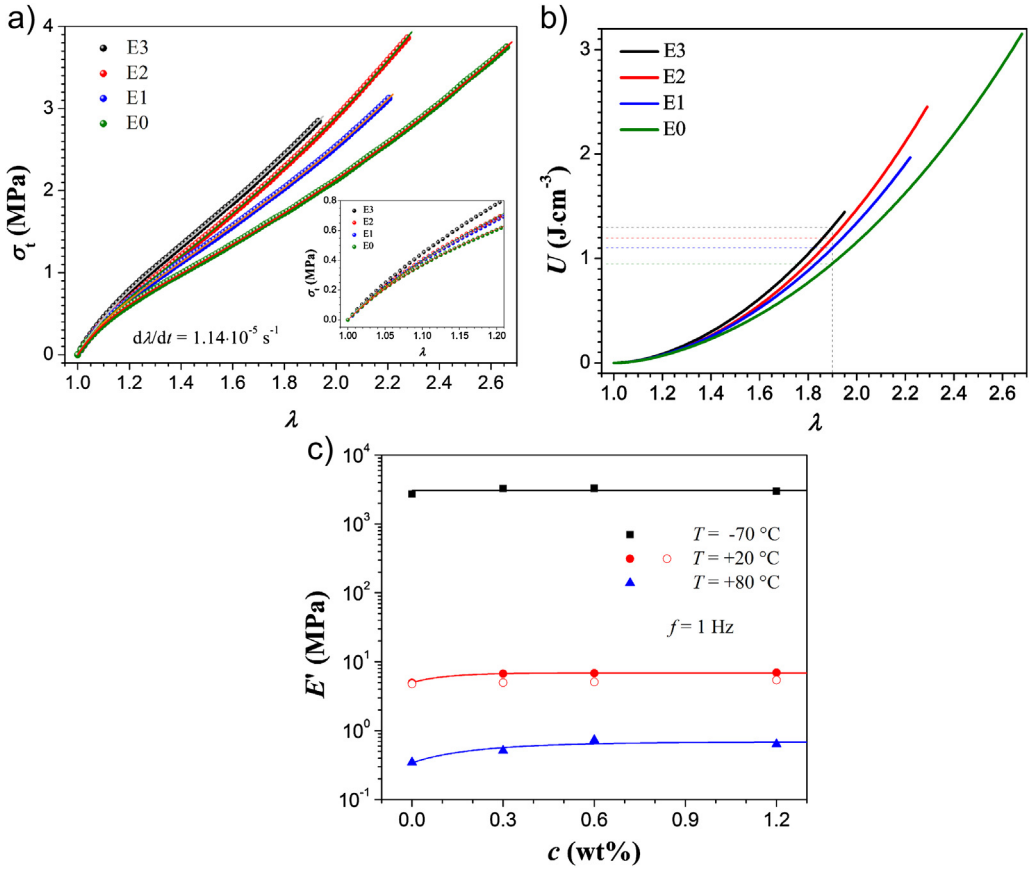

Fig. 7. (a) Uniaxial stress–strain deformation curves and (b) stored elastic energy density for the reference elastomer E0 and the three IOENs E1, E2 and E3 at 20 °C. (c) Storage modulus $E' \approx E$ from the DMA frequency-sweep experiments at different temperatures (full symbols) and elastic modulus from the uniaxial stress–strain experiments at room temperature (empty symbols) as a function of the NPs concentration.

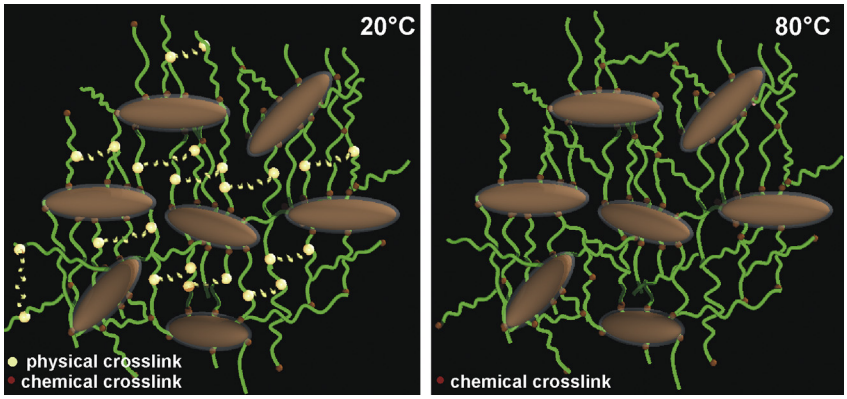

Fig. 8. Schematic representation showing (a) the chemical and physical elastomeric networks at 20 °C with higher crosslinking density, and (b) the only chemical elastomeric network at 80 °C (and back to 20 °C) with lower crosslinking density.

true stress (σ_t) versus strain (λ) curves for the reference samples E0 and the three IOENs, where a clear increase in the mechanical properties of the samples is observed upon increasing the NPs content. Experimental data were fitted by using exponential and linear functions [46], and the corresponding derivative allowed for the evaluation of the initial slope of the fitting curves. The resulting elastic modulus for the four elastomeric samples was $E = 4.77$, 4.97, 5.07 and 5.44 MPa for E0, E1, E2 and E3, respectively. These results confirmed the idea that the elastic modulus of the samples is increased when the content of SCH NPs in the material is also increased. Taking into account the relationship $M_c = 3RTd_{matrix}/E'$ the segmental molecular weight M_c was evaluated from the DMA frequency-sweep experiments. The results show that the estimated molecular weight between crosslinking points, M_c at +20 °C, where both physical and chemical crosslinking are effective, was found equal to 1478, 1087, 1075 and 1053 g mol^{-1} for E0, E1, E2 and E3, respectively, which is in good agreement with the molecular weight of the diamino-terminated polymer Jeffamine D-2000. In comparison after the break of the hydrogen bonding at +80 °C, the same evaluation leads to an estimation of M_c between chemical crosslinkers more than one order of magnitude higher than at +20 °C (25,235, 16,985, 12,099 and 13,800 g mol^{-1} with increasing filler concentration), which is as well more sensitive to the presence of the nanoparticles acting as multivalent crosslinkers.

Moreover, the elastic energy density function (U) was calculated from the stress–strain curves for each IOENs [46]. Fig. 7b shows the increased energy per unit volume at the same strain ratio when the amounts of NPs in the polymer matrix are increased, i.e., a clear indication of the reinforcement induced by the presence of NPs into the polymer network. Fig. 7c displays the storage modulus E' as function of the NPs concentration at different temperatures. Thus, at −70 °C, in the glassy state, an almost constant value for the storage modulus was observed, while at +20 and +80 °C, in the two rubbery states, an increase in the storage modulus appeared when increasing the NPs content. The difference in the storage modulus coming from the two rubbery plateaux is due to the presence of additional hydrogen bonds around room temperature, which bring enthalpy to the samples (Fig. 8). Those hydrogen bonds vanish at high temperatures leading to a chemical network. Moreover, the presence of SCH NPs clearly enhances the mechanical properties of the IOENS in the rubbery state, as can be observed from the trend lines in Fig. 7c.

To summarize, the particles surface chemistry is key parameter for the final dispersion and controlled distribution of the NPs into the matrix, which directly affects the final mechanical properties of the nanocomposite over a large range of temperatures, from −70 to 110 °C. As a consequence, the appropriate surface functionalisation of the NPs not only controls the mutual affinity between the filler and the polymer matrix, but promotes and enhances the mechanical properties even at very low filler concentration.

4. Conclusions

Elastomeric hybrid nanocomposites were obtained by integrating different amounts of surface-functionalised SCH NPs, which were employed as multifunctional chemical crosslinkers. Dispersion, distribution and crosslinking effect of the amino surface-modified NPs within the elastomeric matrix were demonstrated by swelling experiments and SAXS investigations.

The controlled synthetic approach employed here represents a major step towards the development of new high performance nanocomposite materials where the appropriate surface functionalisation of the filler enhanced their compatibility within the matrix leading to nanocomposite materials where aggregation phenomena were avoided.

Mechanical experiments such as uniaxial strain–stress and DMA evidenced the physical and chemical crosslinking contributions in the matrix. The mechanical properties of these covalent networks, which are assisted by supramolecular interactions (hydrogen bonds), were tuneable as a function of temperature. The storage modulus was three orders of magnitude higher than at room temperature when hydrogen bonds formed between the urea motives below the T_g, whereas above 70 °C, when the physical crosslinks (hydrogen bonds) vanished, the storage modulus was about one order of magnitude lower than at room temperature.

It has been shown that the SCH NPs incorporated into the polymer matrix have dual effects as multifunctional crosslinkers and reinforcing fillers, when both the physical and chemical crosslinking contributions are present.

The importance of the filler dispersion quality has mostly been demonstrated from the final properties of the nanocomposites, where low loading of the surface-functionalised SCH NPs (1.2 wt%) increased up to 40% of their mechanical response at 20 °C, and up to 80% at 80 °C after the removal of the physical crosslinking of the polymer matrix. In this sense, improvements on the property of nanocomposite related to the dispersion quality of the filler into the matrix can be achieved by the appropriate selection of particles and matrices, that serves as the starting point towards the development of new functional hybrid materials.

Acknowledgements

The authors acknowledge the financial support provided by the Adolphe Merkle Foundation, ETH Zurich and thank the Swiss

National Foundation NFP62 "*Smart Materials*" for funding the project. We thank Mr. I. Martchenko for the useful discussions on the particles' DLS data. SAXS experiments were performed at the cSAXS beam line (X12SA) of the Swiss Light Source at the Paul Scherrer Institute, Switzerland. We kindly acknowledge the expert help from our local contact Dr. Ana Diaz.

Appendix A. Supplementary data

Supplementary data related to this article can be found at http://dx.doi.org/10.1016/j.polymer.2013.05.056.

References

[1] Behrens S. Nanoscale 2011;3:877–92.
[2] Hsu L, Weder C, Rowan SJ. J Mat Chem 2011;21:2812–22.
[3] Li S, Lin MM, Toprak MS, Kim DK, Muhammed M. Nano Rev 2010;1:5214.
[4] Jestin J, Cousin F, Dubois I, Ménager C, Schweins R, Oberdisse J, et al. Adv Mater 2008;20:2533–40.
[5] Viswanathan V, Laha T, Balani K, Agarwal A, Schweins R, Seal S. Mat Sci Eng R 2006;54:121–285.
[6] Shang S, Zeng W, Tao XM. J Mat Chem 2011;21:7274–80.
[7] Pucci A, Bizzarri R, Ruggeri G. Soft Matter 2011;7:3689–700.
[8] Robbes AS, Jestin J, Meneau F, Dalmas F, Sandre O, Perez J, et al. Macromolecules 2010;43:5785–96.
[9] Satarkar NS, Hilt JZ. Acta Biomater 2008;4:11–6.
[10] Hammond MR, Dietsch H, Pravaz O, Schurtenberger P. Macromolecules 2010;43:8340–3.
[11] Jouault N, Vallat P, Dalmas F, Said S, Jestin J, Boué F. Macromolecules 2009;42:2031–40.
[12] Taschin A, Bartolini P, Sánchez-Ferrer A, Mezzenga R, Mrzel A, Torre R. Sensors Transducers J 2011;12:46–52.
[13] Samulionis V, Banys J, Sánchez-Ferrer A, Mezzenga R. Sensors Transducers J 2011;12:66–70.
[14] Heinrich G, Klüppel M, Vilgis TA. Curr Opin Solid State Mater 2002;6:195–203.
[15] Berriot J, Lequeux F, Montes H, Pernot H. Polymer 2002;43:6131–8.
[16] Stöckelhuber KW, Svistkov AS, Pelevin AG, Heinrich G. Macromolecules 2011;44:4366–81.
[17] Fritzsche J, Klüppel M. J Phys Condens Matter 2011;23:035104–15.
[18] Montes H, Chaussé T, Papon A, Lequeux F, Guy L. Eur Phys J E 2010;31:263–8.
[19] Berriot J, Martin F, Montes H, Monnerie L, Sotta P. Polymer 2003;44:1437–47.
[20] Valentin JL, Mora-Barrantes I, Carretero-González J, López-Manchado MA, Sotta P, Long DR, et al. Macromolecules 2010;43:334–46.
[21] Serbescu A, Saalwächter K. Polymer 2009;50:5434–42.
[22] Ok S, Steinhart M, Serbescu A, Franz C, Chavez F, Saalwächter K. Macromolecules 2010;43:4429–34.
[23] Bistričić L, Baranović G, Leskovac M, Bajsić EG. Macromolecules 2010;46:1975–87.
[24] Starr FW, Schröder TB, Glotzer SC. Macromolecules 2002;35:4481–92.
[25] Douglas JF, Freed KF. Macromolecules 1997;30:1813–7.
[26] Merabia S, Sotta P, Long DR. Macromolecules 2008;41:8252–66.
[27] Mortezaei M, Famili MHN, Kokabi M. Compos Sci Technol 2011;71:1039–45.
[28] Okada A, Usuki A. Macromol Mater Eng 2006;291:1449–76.
[29] Pradhan S, Costa F, Wagenknecht U, Jehnichen D, Bhowmick A, Heinrich G. Eur Polym J 2008;44:3122–32.
[30] Kelarakis A, Yoon K, Somani RH, Chen X, Hsiao BS, Chu B. Polymer 2005;46:11591–9.
[31] Yakacki CM, Satarkar NS, Gall K, Hilt RLJZ. J Appl Polym Sci 2009;112:3166–76.
[32] Schmidt AM. Macromol Rapid Commun 2006;27:1168–72.
[33] Sánchez-Ferrer A, Reufer M, Mezzenga R, Schurtenberger P, Dietsch H. Nanotechnology 2010;21. 185603(1–7).
[34] Sánchez-Ferrer A, Mezzenga R, Dietsch H. Macromol Chem Phys 2011;212:627–34.
[35] Sacanna S, Rossi L, Kuipers BWM, Philipse AP. Langmuir 2006;22:1822–7.
[36] Sánchez-Ferrer A, Rogez D, Martinoty P. Macromol Chem Phys 2010;211:1712–21.
[37] Reufer M, Dietsch H, Gasser U, Hirt A, Menzel A, Schurtenberger P. J Phys Chem B 2010;114:4763–9.
[38] Berr SS. J Phys Chem 1987;91:4760–5.
[39] Sacanna S, Rossi L, Wouterse A, Philipse AP. J Phys Condens Matter 2007;19.376108(1-16).
[40] Perrin F. J Phys Radium 1936;7:1–11.
[41] Martchenko I, Dietsch H, Moitzi C, Schurtenberger P. J Phys Chem B 2011;115:14838–45.
[42] Griffete N, Clift MJD, Lamouri A, Mihut AM, Fink A, Rothen-Rutishauser B, et al. Colloids Surf A 2012;415:98–104.
[43] Diamant Y, Folman M. Polymer 1979;20:1025–33.
[44] Le Gal A, Yang X, Klüppel M. J Chem Phys 2005;123:014704.
[45] Klüppel M. J Phys Condens Matter 2009;21:035104.
[46] Sánchez-Ferrer A, Finkelmann H. Mol Cryst Liq Cryst 2009;508:348–56.